Ebb-dominant mixing increases the seaward sediment flux in a stratified estuary

I. Niesten[1], Y. Huismans[2,3], A.J.F. Hoitink[1]

[1]Department of Environmental Sciences, Hydrology and Environmental Hydraulics, Wageningen University, Wageningen, The Netherlands
[2]Marine and Coastal systems, Applied Morphodynamics group, Deltares, Delft, The Netherlands
[3]Civil Engineering and Geosciences, Delft University of Technology, Delft, The Netherlands

Key Points:

- Residual sediment transport in a time-dependent salt wedge estuary is governed by barotropic and internal tidal asymmetry.
- Ebb-dominant tidal mixing increases the seaward sediment transport, as sediment resuspension extends further to the surface compared to the flood phase.
- Shear-induced entrainment of sediment-rich marine water further increases the seaward sediment flux, although the effect of this mechanism is small.

Corresponding author: Iris Niesten, `iris.niesten@wur.nl`

Abstract

Intratidal variability in stratification, referred to as internal tidal asymmetry, affects the residual sediment flux of an estuary by altering sediment transport differently during ebb and flood. While earlier studies suggest that flood-dominant mixing increases the residual landward sediment flux, the role of ebb-dominant mixing remains largely unknown. Based on field data, we investigate the mechanisms that cause ebb-dominant mixing and its effect on the residual sediment flux in a stratified estuarine channel. Observations based on two tidal cycles show that the pycnocline remains largely intact during flood. Vertical mixing during flood is inhibited by a strong fresh water outflow, confining landward transport of suspended sediment to the bottom layer. During ebb, the pycnocline height decreases until it interacts with the bottom boundary layer, resulting in enhanced vertical mixing and sediment transport extending further to the surface. Thus, ebb-dominant mixing increases the residual sediment flux in seaward direction. The long ebb period further contributes to the residual ebb-flux. This is noteworthy since a long ebb duration, as it corresponds to flood dominance, is often associated with a landward residual sediment flux. Although our data represent average conditions and may not be representative for high river discharge or storm conditions, we conclude that asymmetries in vertical mixing considerably affect the residual sediment flux.

Plain Language Summary

Sediment is supplied to estuaries by the upstream river discharge and, depending on the tidal properties, by the downstream inflow of seawater. Whether an estuary loses or gains sediment through the seaward boundary, depends on several processes. Based on field data, here we investigate the effect of mixing between fresh river water and saline seawater. Sediment is transported landward during flood (import) and seaward during ebb (export). During flood, the water is vertically layered, consisting of a lower layer of saline water and a surface layer of fresh water, which are largely decoupled from each other. As a result, sediment from the sea is transported by the bottom layer only. During ebb, the saline and freshwater layers are better mixed and sediment is transported by both layers. This results in a larger sediment transport capacity in seaward direction, increasing sediment export from the estuary. Another process that increases sediment export is the inequality between ebb duration and flood duration. Since the ebb period is several hours longer than the flood period, more sediment is allowed to be transported seaward.

1 Introduction

Estuarine morphodynamics are to a large extent determined by residual sediment transport. In tide-dominated deltas, the residual sediment transport largely depends on tidal hydrodynamics. As a tidal wave enters an estuary, its shape is deformed by width and depth convergence, bottom friction and interaction with the river flow. In many estuaries, this leads to flood-dominance, i.e. a shorter flood duration but stronger flood currents compared to the ebb currents. Flood-dominance is often associated with relatively shallow estuaries with limited intertidal area (Pugh & Woodworth, 2014). Intertidal flats tend to reduce flood flow velocity leading to ebb-dominance in estuaries with a large intertidal area. As transport of sediment scales non-linearly with flow velocity, a small difference between ebb and flood currents can cause a significant difference in residual sediment transport (e.g. Dronkers (1986); Wang et al. (2002)).

The main mechanisms leading to sediment import in estuaries are well-known and described by Burchard et al. (2018). The two most important mechanisms contributing to a landward sediment flux are gravitational circulation (Burchard et al., 2018; Dyer, 1995) , where a salinity gradient in longitudinal direction results in a residual landward current near the bed, and flood tidal asymmetry (Burchard et al., 2018; Dronkers, 2005;

Wang et al., 2002). Other mechanisms such as lateral and topographic trapping are system-specific. The main mechanisms associated with sediment export, i.e. seaward residual sediment transport, include flushing by river discharge (e.g. Guo et al. (2014); Canestrelli et al. (2014)) and ebb-dominance (Guo et al., 2018).

The prediction of residual sediment transport in estuaries is complicated by the presence of density gradients and density stratification. Jay and Musiak (1996) distinguish between barotropic tidal asymmetry and internal tidal asymmetry, the former being defined as an asymmetry in flood and ebb maximum currents and water level duration, and the latter as variations in stratification on a sub-tidal timescale. It is argued that for the Columbia river, the residual current induced by internal tidal asymmetry is a main driver of landward sediment transport. Simpson et al. (1990) describe how the asymmetry in vertical mixing is enhanced by tidal straining, and hypothesize that this may contribute to a landward flux of salt. Similarly, Scully and Friedrichs (2003) observe a landward residual sediment flux in the York River Estuary despite the residual currents being directed seaward, and attribute this to vertical mixing being suppressed by a stable pycnocline formed during the ebb tide. During flood tide, mixing causes suspended sediment to occur higher in the vertical, resulting in a large landward transport capacity during flooding.

While descriptions of systems with flood-dominant mixing are abundant in literature (Jay & Musiak, 1996; Scully & Friedrichs, 2003, 2007; Stacey et al., 1999), some estuaries show an opposite behaviour where the flood flow tends to stabilize stratification and the ebb flow destabilizes the water column. Schijf and Schönfeld (1953) already hypothesized that interfacial instability combined with bed friction may corrupt a salt wedge during the ebb tide. Geyer and Farmer (1989) observed increased shear instability in the Fraser River Estuary during ebb, leading to a collapse of the salt wedge, and Geyer et al. (2008) and Ralston et al. (2010) describe how increased mixing in the bottom boundary layer is the primary cause for the collapse of the salt wedge during ebb in the Merrimack River Estuary. This ebb-dominant mixing is primarily associated with highly stratified or salt-wedge estuaries, where a strong freshwater outflow counteracts tidal mixing during flood (Geyer & Ralston, 2011).

The effect of mixing on residual sediment and salt fluxes has been investigated for multiple mixed and partially stratified estuaries, such as the Columbia River Estuary (Jay & Musiak, 1996), the York River Estuary (Scully & Friedrichs, 2007) and the Navesink River Estuary (Chant & Stoner, 2001). Here, we demonstrate the importance of mixing for the residual sediment transport in an ebb-dominant, highly stratified system. The aim of our work is to 1) establish and understand the processes controlling mixing in a stratified estuarine channel, and 2) to assess its effect on residual sediment transport.

Measurements were carried out in the Rotterdam New Waterway, The Netherlands. The New Waterway is a 10-km long channel in the Dutch Rhine-Meuse Delta, which features no lateral outflows and harbors. It is a heavily engineered, deep channel, which can be characterized as a time-dependent salt-wedge estuary in the framework of Geyer and MacCready (2014), under average conditions. de Nijs et al. (2011) describe how the internal flow structure in the New Waterway is governed by advection of the salt wedge and states that the classical theory of tidal straining cannot explain the temporal variations in turbulence. Previous sediment budget studies (Cox et al., 2021; Frings et al., 2019) hypothesized a large import of marine mud and sand through the mouth, which is attributed to the landward residual current near the bed.

The remainder of this paper is structured as follows. Chapter 2 describes the study area in more detail, and offers a description of the field measurements and data processing methods. Chapter 3 presents the most important findings concerning vertical mixing and sediment transport. Then, Chapter 4 discusses the implications of our findings

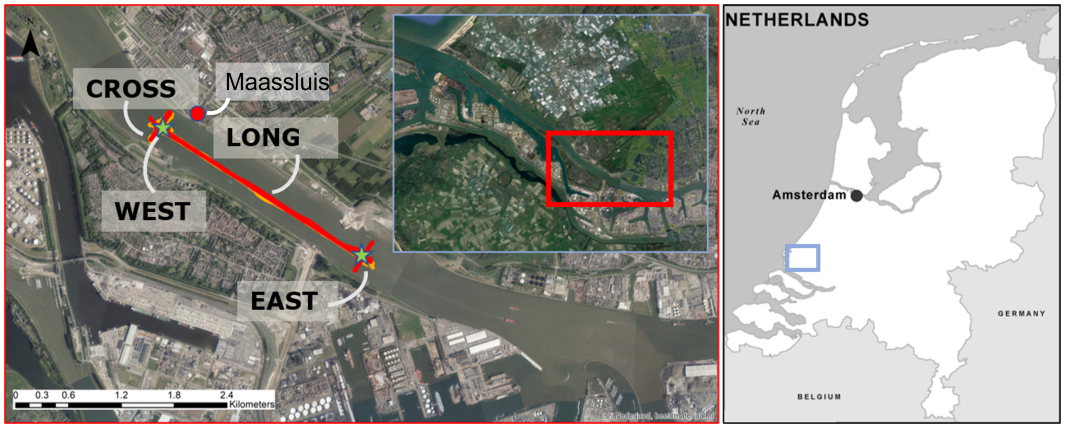

Figure 1. Overview of the survey area and its location in the New Waterway. Orange and red lines indicate the moving-boat measurements. The locations of the Eastern and Western point measurements are indicated by a star.

for the residual sediment flux, and modeling of sediment transport in stratified systems and delta formation. Chapter 5 summarizes the main conclusions.

2 Materials and methods

2.1 Study area

The New Waterway connects the Rhine-Meuse Delta (RMD) to the North Sea (Figure 1). The RMD is located in the west of the Netherlands and is fed by the Meuse river and by two main branches of the Rhine river, referred to as the Waal and Lek. Water is discharged into the North Sea via two deltaic channels: the New Waterway in the north and the Haringvliet in the south. Of these channels, the Southern Haringvliet is partly closed off since 1970, and its discharge is now controlled by a complex of sluices, which greatly affected the water levels (Vellinga et al., 2014), tidal currents and sedimentation and erosion in the branches (Huismans et al., 2021). Under average discharge conditions, a net discharge of about 220 m^3/s reaches the North Sea via the Southern Haringvliet branch, while the Northern New Waterway discharges about 1400 m^3/s (Cox et al., 2021). During periods of low river discharge, the Haringvliet sluices are closed, and all river discharge leaves the system via the New Waterway. The tidal motion in the New Waterway is determined by the tides at Hoek van Holland. The tidal regime is predominantly semi-diurnal and flood-dominant. Tidal ranges vary between 2.0 m (spring tide) and 1.2 m (neap tide), under average conditions (De Nijs, 2012).

The New Waterway has been deepened considerably over the past decades (Vellinga et al., 2014; Cox et al., 2021), leading to a deep and almost prismatic channel. The New Waterway has a depth of approximately 17 m and a width of about 500 m. A strong gravitational circulation has been suggested to drive a large import of both sand and silt (Cox et al., 2021). The bed material of the New Waterway mainly consists of fine and medium sand, as the channel hydrodynamics are too strong to allow for siltation of finer material. Bed material in the upstream harbour basins, however, contains predominantly fine silt and mud. (De Nijs, 2012).

2.2 Survey set up and hydrodynamic conditions

Two 13-hour boat surveys were carried out in the channel, about 10 km upstream of the estuary mouth. The first survey took place on 8 March 2021 during neap tide. The

second survey took place on 15 March 2021 during spring tide. Rhine discharge (measured upstream at Lobith station near the German border) varied between 1900 m^3 s^{-1} and 2100 m^3 s^{-1} during the week preceding the first survey until the day of the second survey, which is close to the average discharge of about 2200 $m^3 s^{-1}$. Wind speeds were low (5 and 9 m/s, respectively) during the two surveys, corresponding to zero set-up during the first measuring day and an average set-up of 26 cm during the second measuring day at the estuary mouth (Figure 2). Summarizing, the conditions during the measurements represent average conditions with limited setup and a near-average river discharge. Figure 1 provides an overview of the survey location. One vessel, equipped with a 600 kHz and a 1200 kHz ADCP collected continuous velocity and backscatter profile data over a longitudinal trajectory of 2.8 km. The sailing time of the longitudinal trajectory amounts approximately 20 minutes. The location of this trajectory was chosen such that no lateral effects from side channels or port basins are expected. Additional hourly velocity and backscatter profile data were collected along a cross-sectional trajectory, located at the downstream end of the longitudinal trajectory. Furthermore, two measuring locations (EAST and WEST) were defined at both endpoints of the longitudinal trajectory. The western measuring location coincides with the cross-sectional trajectory. At both measuring locations, hourly depth casts were carried out collecting vertical profiles of salinity, turbidity and sediment concentration.

Each 13-h measurement cycle consists of the following measurements: starting at the most downstream measuring location (WEST), a measuring frame equipped with a SeaPoint OBS, a CTD-sensor and a LISST-100x is deployed to collect a full depth profile. Additional water samples are collected at 3 depths using Niskin bottles, to calibrate the OBS and ADCP backscatter intensity to SSC. After collecting depth profile data with the measurement frame, the cross-section transect was sailed at the western location to collect ADCP data. This was followed by the longitudinal trajectory of 2800 m following the channel center line, collecting ADCP data over the full trajectory. Arriving at the eastern location, another depth profile is sampled with the measuring frame. Subsequently, ADCP data were collected again along the longitudinal trajectory and, arriving at the western location, the measurement cycle would start over again. Water level data were available at a nearby measuring station ("Maassluis", see figure 1) with a 10-minute measuring frequency.

2.3 Data pre-processing

2.3.1 Salinity and density

The CTD sensor measures conductivity as a proxy for salinity. The combined measurements of conductivity and chloride concentration at a nearby permanent measuring station (Hoek van Holland) were used to establish a relation between measured conductivity and salinity in the New Waterway, with $S = 1.80655 \cdot Cl$, with S the salinity in ppt and Cl the concentration of chloride in g/L. The relation between conductivity (C in S/m) and salinity is:

$$S = 8.56 \cdot C^{1.16} \tag{1}$$

The water density relates to both salinity and temperature according to the equation of state for sea water (UNESCO/IOC, 2010).

2.3.2 Tidal currents inferred from ADCP data

The ADCP-data are split into 2 spatial transects: one cross-sectional transect, covering the full channel width (about 400 m) at the location of the western measurement point, and one longitudinal transect, covering the channel centerline over a length of 2.8 km. A mesh is defined for both transects following the method of Vermeulen et al. (2014), on which velocity and backscatter data are projected. The cell size (width x height) of the cross-sectional mesh is approximately 10x0.5 m and the cell size of the longitudinal

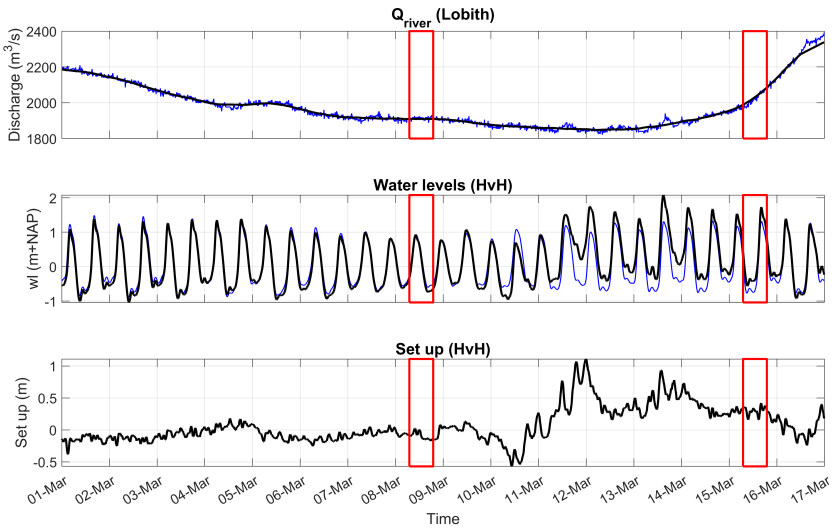

Figure 2. Hydrodynamic conditions during the measuring period. Upper panel: upstream river discharge (blue) and its daily average (black). Middle panel: astronomical tide (blue) and measured water levels (black) at the estuary mouth. Lower panel: water level due to wind set-up at the estuary mouth. Red boxes indicate the time windows during which was measured.

mesh is 50x0.5 m. Adopting the method of Vermeulen et al. (2014), radial velocity measurements are assigned to a mesh cell based on their location. All velocity measurements in one mesh cell are subsequently inverted to obtain either a mean velocity vector, or coefficients of a function in time that is fitted to the data. Recently, Jongbloed et al. (2023) extended and refined this method for ADCP data processing. Using their method for tidal applications, all radial velocities within one mesh cell, measured throughout the 13-h cycle, are fitted to a time-dependent model equation, retrieving the phases and amplitudes of dominant tidal species and the residual flow. Spectral analysis of modeled flow velocities (Leuven et al., 2023) confirms that in the New Waterway the M_2-component is dominant, followed by M_4 and M_6. Velocity in all directions is thus fitted to the following function:

$$\begin{aligned} u_i = \mathbf{u}_0 + \mathbf{A}_{M2}\cos(2\pi/T_{M2}t) + \mathbf{B}_{M2}\sin(2\pi/T_{M2}t) + ... \\ \mathbf{A}_{M4}\cos(2\pi/T_{M4}t) + \mathbf{B}_{M4}\sin(2\pi/T_{M4}t) + ... \\ \mathbf{A}_{M6}\cos(2\pi/T_{M6}t) + \mathbf{B}_{M6}\sin(2\pi/T_{M6}t) \end{aligned} \quad (2)$$

where u_i represents the velocity (m s^{-1}) or its derivative in any direction (m s^{-1} or s^{-1}). $\mathbf{u}_0$ is the residual velocity or its derivative, T_{Mn} (d) the period of the tidal harmonic with a period that corresponds to n cycles per day. The amplitudes and phases of those harmonics equal $\sqrt{\mathbf{A}_{Mn}^2 + \mathbf{B}_{Mn}^2}$ and $\tan^{-1}(\mathbf{B}_{Mn}/\mathbf{A}_{Mn})$, respectively. Following Jongbloed et al. (2023), the residual velocity $\mathbf{u}_0$ and parameters $\mathbf{A}_{Mn}$ and $\mathbf{B}_{Mn}$ result from a physics-informed regularization procedure. Five physics-based constraints are taken into account in the regularization procedure: 1) conservation of mass within a mesh cell, 2) conservation of continuity in between cells, 3) coherence between cells (limiting spatial fluctuations of the Reynols-averaged flow), 4) consistency between cells (intra-cell partial derivatives should equal central differences across cells) and 5) kinematic boundary conditions (no flow through the bottom and surface). Using a machine-learning based approach, the Reynolds-averaged velocity field retrieved from the ADCP radial velocity data is an optimal solution that satisfies those constraints as good as possible. We applied the method of Jongbloed et al. (2023) to solve the three-dimensional velocity vector (u, v, w)

and its first order derivatives in the (x, y, σ)-space, using the default set of penalty parameters for the five physics based constraints ($\boldsymbol{\lambda}$), i.e. $[\lambda_1, \lambda_2, \lambda_3, \lambda_4, \lambda_5] = [100, 100, 5, 5, 100]$ (Vermeulen & Jongbloed, 2023), implying that the relative importance of the coherence and consistency constraints is small compared to that of the other constraints.

2.3.3 Quantifying vertical mixing

Layer definition and mixing layer thickness

All CTD casts were analyzed to define an upper and lower layer, separated by the pycnocline. First, all conductivity data were converted to salinity, following the procedure described above. Repeated casts (defined as subsequent casts with a maximum time interval of 5 minutes) were combined and treated as a single cast. The data were filtered to remove the upper 0.5 m of every cast to exclude erroneous data induced by air bubbles. No smoothing was applied. The pycnocline is defined as the height of the maximum vertical density gradient. To find the height of the pycnocline (z_i) and the salinity at the pycnocline ($s_{z(i)}$), all obtained salinity profiles were described by a sigmoid function:

$$s(z) = s_{z(i)}\left(1 - \tanh\left(\frac{z - z_i}{\delta_z/2}\right)\right) + s_{min} \tag{3}$$

where $s(z)$ is salinity as a function of elevation above the bed, δ_z a measure of the mixing layer thickness and s_{min} the offset of the function, defined as the minimum measured salinity. We fitted equation 3 to all salinity-depth casts to obtain the interface height, its corresponding salinity and the mixing layer thickness. The resulting profiles are provided in figures A1 and A2.

Internal shear

Shear instability is known to be one of the primary mechanisms causing mixing of salt stratified flows (Geyer & Farmer, 1989), yet it remains hard to estimate shear from field data due to its sensitivity to the velocity gradient. The method of Jongbloed et al. (2023) allows for an accurate, yet smooth estimate of the velocity derivatives in all directions, which would otherwise be hardly visible from the raw data. Therefore, we use the velocity model described with equation 2 to quantify vertical shear.

Richardson gradient number

As a last proxy for interfacial mixing, we calculate the gradient Richardson number (following e.g. Richardson and Shaw (1920); Miles (1961)) which represents the ratio of the stabilizing density gradient (if positive) and the de-stabilizing shear stress. The gradient Richardson number is defined by:

$$Ri_g = \frac{g}{\rho_0}\frac{\partial\rho/\partial z}{\partial^2 u/\partial z^2} \tag{4}$$

It has been theoretically shown that a water column is vertically stable when $Ri_g > 1/4$. When Ri_g falls below 1/4, shear instabilities initiate mixing (e.g. Miles (1961); Trowbridge (1992)). The local vertical density gradient is defined by the sigmoid function in equation 3, which is interpolated between consecutive casts. A bulk version of the Richardson number is calculated as:

$$Ri_b = \frac{g}{\rho_0}\frac{\Delta\rho/\Delta z}{(\Delta u/\Delta z)^2} \tag{5}$$

with $\Delta\rho/\Delta z$ the top to bottom density difference over the internal mixing layer and $(\Delta u/\Delta z)$ the average shear. The boundaries of the mixing layer are calculated following the procedure described in section 2.3.3, with the upper and lower boundary equal to the pycnocline height plus and minus the mixing layer half width ($z_{mix,top} = z_i + \delta_z/2$ and $z_{mix,bot} = z_i + \delta_z/2$).

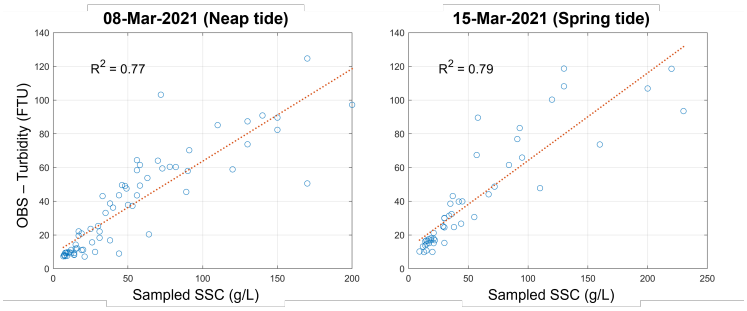

Figure 3. The relation between acoustic backscatter and sampled SSC fits a simple power law.

2.4 SSC from acoustic backscatter

The ADCP echo intensity profiles were transformed into volume backscattering strength S_v using the sonar equation as proposed by Gostiaux and van Haren (2010). Ignoring the effect of sound attenuation due to sediment and assuming a vertically constant grain size, the volume backscatter strength is a function of the mass concentration of suspended particles M and a constant representing the scattering properties of the suspended particles k_s, which depends on the particle shape and size (Sassi et al., 2012). Next, the suspended mass concentration can be inferred from the volume backscatter strength using a simple power law fit. The assumption that scattering properties did not significantly change over time was supported by additional samples from which the particle size distribution was determined. In all 15 samples collected during neap tide, the value of D_{50} was consistently between 7.5 and 8.5 μm. The value of D_{50} during spring tide was only slightly larger, ranging between 8 and 10 μm. Applying the correction of Sassi et al. (2012) for sound attenuation from scatter by suspended sediment did not improve the calibration result. Therefore, we adopted a simple power law to derive the suspended concentration SSC from the volume backscatter strength: $SSC = 10^3(10^{\alpha S_v + \beta})$, with SSC the suspended sediment concentration in g/L and α and β calibration coefficients. Before calibration, a filter was applied to remove outliers in the backscatter intensity as a result of air bubbles near the water surface. The power law coefficients were determined for the neap and spring tidal cycles separately. The calibration result of both tidal cycles is shown in figure 3.

2.5 Calculation of residual sediment transport

Apart from the instantaneous sediment flux, the residual flux is calculated over both surveyed tidal cycles. Calculation of the residual flux is based on data measured along the cross-sectional transect, as the cross-section covers the full channel width. The cross-sectional residual sediment flux ($Q_{s,residual}$) is calculated as the sum of the residual sediment fluxes in the individual mesh cells, which equals for every individual cell:

$$Q_{s,residual} = \int_0^T Q_s(t)\ \mathrm{dt} = \int_0^T Q(t) \cdot SSC(t)\ \mathrm{dt} \tag{6}$$

with $Q(t)$ the discharge and $SSC(t)$ the suspended sediment concentration in a mesh cell as a function of time. The integral bounds cover a complete M_2 tidal period. The hourly measured SSCs at the cross-section were interpolated using spline-fitting. Since the backscatter profiles do not extend to the region near the channel bed, sediment transport in the lower 1 m was obtained by extrapolation of the calculated flux in the lower 3 m, assuming zero transport at the bed (no-slip condition).

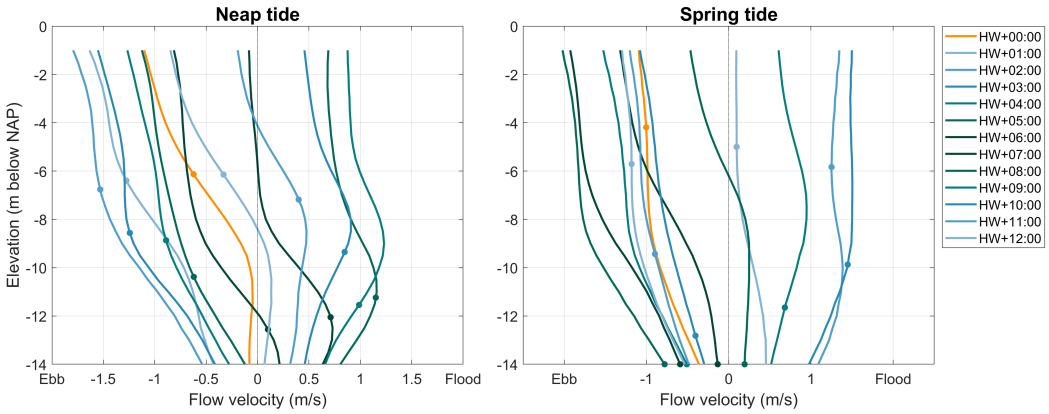

Figure 4. Hourly along-channel velocity profiles during the neap (left panel) and spring tidal surveys (right panel). Every profile is the spatial average along the longitudinal transect indicated in figure 1. Markers along the velocity profile indicate the height of the pycnocline at the downstream (west) side of the transect.

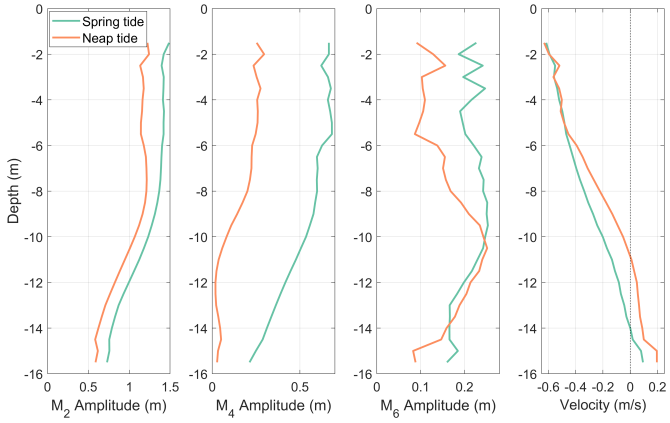

Figure 5. Result of the tidal fit for along-channel velocity component for the neap (orange) and spring (blue) tidal surveys. All results are averaged over the longitudinal transect.

3 Results

3.1 Mean flow and dynamics of the salt wedge

The measured velocity profiles (Figure 4) clearly show the tidal duration asymmetry. During both neap tide and spring tide, the ebb-flow period lasts for 7-8 hours of the total M_2-cycle, corresponding to the tidal duration asymmetry which is observed in the water level time series (figure 2). The velocity profiles of the neap tidal cycle indicate a decoupling between the upper freshwater layer and lower saline water layer, with currents in the lower layer often flowing in opposite direction compared to the upper layer flow direction. Only during late ebb, this decoupling is less pronounced, although the velocity profile is strongly sheared in the vertical. The start of flood in the lower layer precedes flood in the upper layer with about 1 hour. As the flood flow evolves, the velocity maximum shifts from the bottom to mid-depth. This mid-depth velocity maximum corresponds to the flood tidal advection of the salt-wedge into the channel (de Nijs & Pietrzak, 2012). Velocity profiles during the spring tidal cycle are more uniform, but

still show the mid-depth velocity maximum during flood and the strong vertical shear during the late ebb. The pycnocline height, defined as the height of the median salinity (z_i in equation 3), moves vertically upward during flood and downward during ebb (Figure 4) as a result of the advection of the salt wedge. The elevation of the pycnocline above the bed is especially dynamic during spring tide, when it varies between -4 m+NAP around HW and approaches the bottom height during LWS, indicating well-mixed conditions. During neap tide, the pycnocline height varies between -6 and -12 m+NAP. During both tidal cycles, the pycnocline height increases rapidly during flood due to the strong baroclinic forcing.

The analysis described in section 2.5 yields the residual velocity and the amplitude and phase of each tidal component during the neap tidal cycle and spring tidal cycle. The resulting amplitudes of the along-channel velocity are presented in figure 5. The M_2-component accounts for the major part of the streamwise flow variations. The M_2-amplitude of the spring tidal cycle (ranging from 0.7 - 1.4 m/s) is on average 20% larger than the amplitude of the neap tidal cycle (ranging from 0.6 - 1.2 m/s). For both tidal cycles, the M_2-amplitude is fairly constant along the upper half of the water column, but decreases rapidly with depth between mid-depth and the bottom. The top to bottom phase difference can exceed 15° (0.5 hour), for the neap tidal cycle. The depth variation of the M_4-overtide is similar to that of the M_2-component, and its amplitude is smaller: ranging from 0.02 - 0.27 m/s for neap tide and from 0.2 - 0.68 m/s for spring tide. The M_6-amplitude peaks at 0.25 m/s for both tidal cycles. The M_6-amplitude peaks around -10 m (neap tide) and -8 m (spring tide). The clear presence of the M_4- and M_6-overtides indicate a strong asymmetry in tidal currents and mixing.

The residual flow velocity reveals a typical gravitational circulation, with landward residual currents near the bed and seaward residual currents near the surface for both the neap and spring tidal cycles. The height of zero residual velocity is located lower for spring tide than for neap tide, indicating stronger mixed conditions during the spring tidal cycle. The residual currents near the surface (0 to 5 m below MSL) of the neap tidal cycle and spring tidal cycle are comparable. From 5 m-MSL and lower, the spring residual velocity is larger than the neap residual velocity. As a result, the seaward residual current is stronger over the measured spring tidal cycle compared to the neap tidal cycle.

3.2 Mixing asymmetry

We quantify the degree of mixing based on the mixing layer thickness and the bulk Richardson number. The results of the salinity profile fitting procedure based on equation 3 yields the pycnocline height with respect to the bottom height. A complete overview of the results, including all profile fits, can be found in figure A1 for neap tide and figure A2 for spring tide. During neap tide, the internal mixing layer thickness is smallest in the period after HWS, corresponding to more stratified conditions. The mixing layer thickness increases during ebb until it reaches its maximum thickness around LW, which relates to the strong vertical shear around the pycnocline observed in figure 4. Noteworthy is the sudden thickness increase at the Eastern location at $t = \mathrm{HW}{+}02:35\mathrm{h}$, followed by a thickness decrease. The mixing layer thickness at the Western measurement point shows the same widening and narrowing with a time-lag of half an hour compared to the measurement at the Eastern location. The celerity of this disturbance corresponds to the flow velocity at that time, indicating that the temporal widening is most likely caused by layer instability further upstream and advected seaward during the time of measuring.

Results from de Nijs et al. (2011) show that barotropic advection is the main mechanisms driving tidal displacement of the salt wedge, and that vertical mixing is limited throughout most of the tidal cycle. Our results confirm that the surface and bottom layer

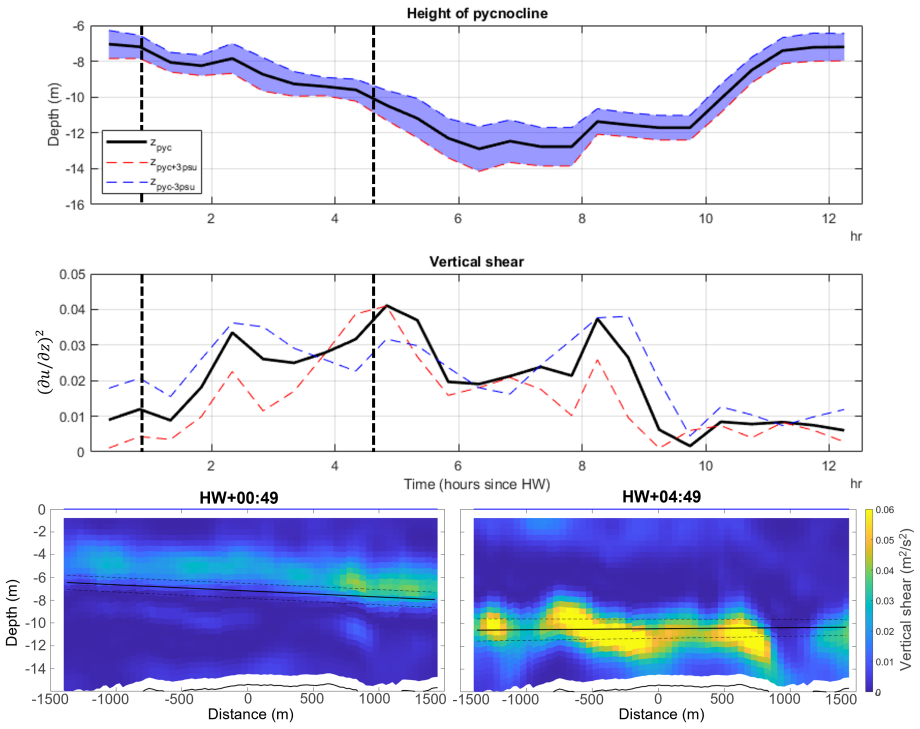

Figure 6. Mixing during the neap tidal cycle. The upper panel shows the development of the pycnocline and height interval where $s = s_{pyc} \pm 3\ psu$. The middle panel shows the vertical shear squared $(\partial u^2/\partial^2 z)$ along and around the pycnocline. Values in the upper two panels are the along-channel average. The vertical lines in the upper two panels indicate the time of the along-channel transects shown in the lower two panels.

are largely decoupled during flood. Around HW, vertical shear along the pycnocline is limited, resulting in a stably stratified flow structure (figure 6 HW+00:49). However, we observe strongly sheared velocity profiles during maximum ebb and late ebb, resulting in diahaline mixing in this period and a decrease of the density gradient at the pycnocline height (figure 6). As the ebb flow progresses, the pycnocline height decreases as a result of the retreating salt wedge, while at the same time, bottom-induced turbulence increases as a result of increasing near-bed currents. Around 4-5 hours after HW, vertical shear at the pycnocline is maximum and the vertical density gradient at the pycnocline starts to decrease (figure 6 HW+04:49). During the long LW-period, the pycnocline has lowered enough to interact with the bottom-induced shear layer, and the thickness of the mixing zone increases, indicating vertical mixing between the upper and lower layers.

The internal mixing layer during the spring tidal cycle shows a similar pattern of thickness increase during ebb and thickness decrease during flood, but the degree of mixing varies more. Similar to neap tide, the mixing layer thickness is at its minimum between maximum flood and maximum ebb (figures 7 and A2: t=HW+10:30 to HW+03:30 hours). Around maximum ebb (figure 7: t=HW+03:10 hours), bed shear increases which initializes vertical mixing through the pycnocline. Already at the start of LWS (around t=HW+05:10 hours), the water column destratifies, as saline water is pushed seaward and the mixing layer height decreases until it approaches the height of the bottom boundary layer (Dyer, 1991). The water column remains well-mixed during the long period around LW and the start of the flood. As the flood phase progresses, and the salt wedge is advected landward, the py-

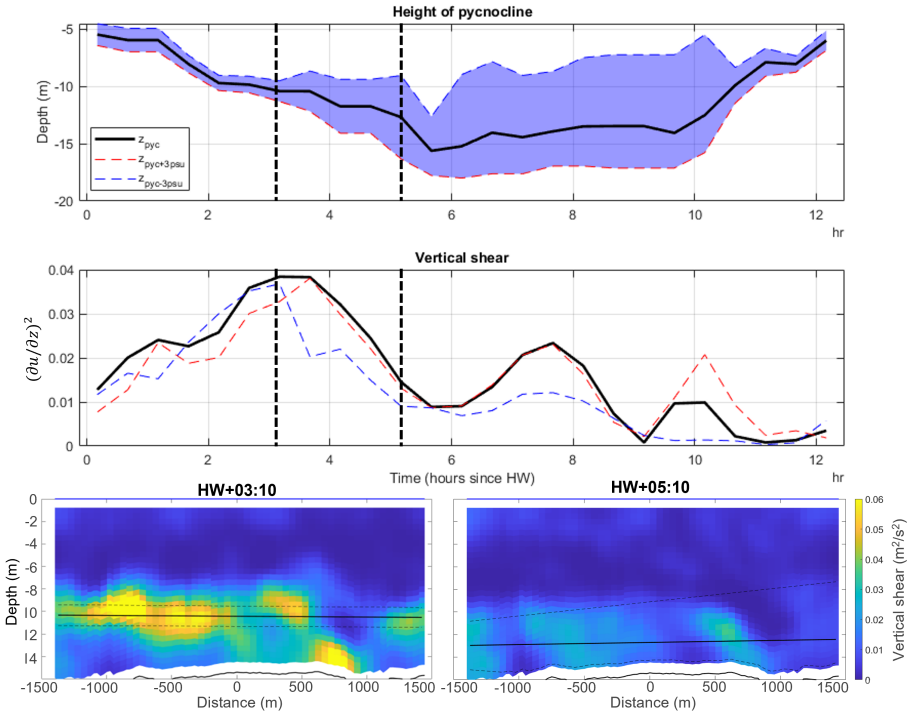

Figure 7. Mixing during the spring tidal cycle. The upper panel shows the development of the pycnocline and height interval where $s = s_{pyc} \pm 3\ psu$. The middle panel shows the vertical shear squared $(\partial u^2/\partial^2 z)$ along and around the pycnocline. Values in the upper two panels are the along-channel average. The vertical lines in the upper two panels indicate the time of the along-channel transects shown in the lower two panels.

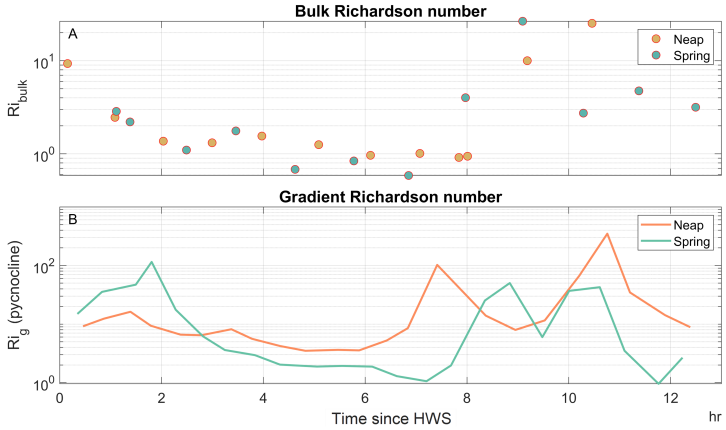

Figure 8. Development of longitudinal transect-averaged bulk Richardson numbers during neap tide and spring tide (upper panel) at the Western measuring location. Lower panel shows the time-varying Richardson gradient number at the pycnocline height for neap tide and spring tide, averaged over the longitudinal transect. Time is in hours since HW.

cnocline height increases and the water column again shows a strong stratification around the time of maximum flood (t=HW+10.30 hours).

The temporal variation of the Richardson number (figure 8) supports the observations of ebb-dominant mixing during either of the two tidal cycles subject to study. Both during the neap tidal cycle and during the spring tidal cycle, Ri_b-values are lowest towards the end of the ebb phase. This confirms that mixing is most intense during ebb. Both bulk (figure 8: panel A) and gradient Richardson numbers (figure 8: panel B) are relatively high. Ri_g-values at the pycnocline are never below 0.25. This suggests that mixing is caused by larger-scale instabilities.

3.3 Time-varying transport of suspended sediment

Figures 9 and 10 show the measured backscatter profiles converted to suspended sediment concentration (SSC) along the repeated longitudinal transect as a single time-series (measurements along separate transects are included in appendix Appendix B. During the flood phase of the neap tidal cycle, suspended sediment is confined below the pycnocline, which corresponds to the intensified stratification that develops during flood and persists until the beginning of the ebb phase in this period. As a result of confinement during flood, sediment import is restricted mostly to the bottom layer. In the early ebb phase (12:30 - 13:00), patches of elevated SSC levels are present in the upper layer, while at the same time SSCs in the bottom layer decrease as a result of decelerating flow velocity (figure 9). The top-layer SSC peaks seem to originate from outside the measurement area, and persist while being transported. The longer ebb phase is characterized by lower near-bed SSCs compared to flood, and higher top-layer SSCs compared to flood. This can be explained from the increase in vertical mixing as observed, and contributes to sediment export.

Suspended sediment dynamics during the spring tidal cycle show a similar pattern, but in general concentrations are higher (figure 10). Similar to neap tide, patches of high SSC in the top layer are observed after HW (figure 10). High near-bed SSCs are observed both during maximum flood and maximum ebb, although SSCs are better mixed over the vertical during ebb tide. The latter agrees with the observed increase in mixing layer

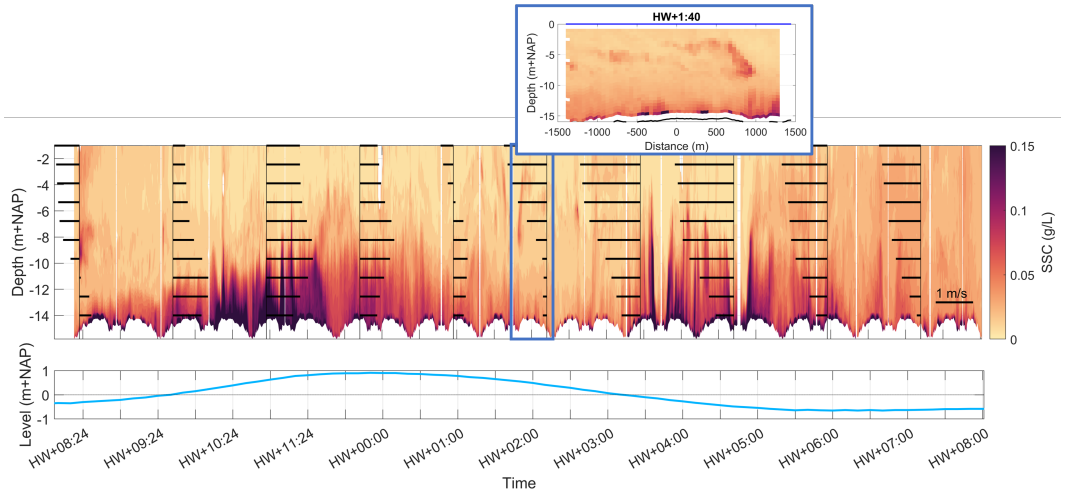

Figure 9. Tidal currents and suspended sediment concentration (top panel) as measured during the neap tidal cycle. Corresponding water levels are provided in the lower panel. An inset shows the elevated SSC's in the upper water layer at the start of the ebb phase.

thickness (figure 7 and salinity profiles in figure A2). Around t=HWS+05:00h, the mixing layer thickens, followed by a break-down of the salinity structure. As a result, sediment export takes place both in the bottom layer and in the surface layer during ebb, while sediment import is concentrated in the bottom layer during flood tide.

3.4 Contribution of the bottom and surface layer

Figures 11 and 12 show the time-varying sediment transport in top and bottom layers throughout the neap and spring tidal cycles respectively. Due to the combined effects of gravitational circulation and sediment resuspension from the bed, import in the bottom layer exceeds import in the top layer at any time, even though flow velocity is usually higher in the top layer. During flood in both the neap and spring tide surveys, suspended sediment is mostly confined below the pycnocline, which explains low sediment import across the top layer. During ebb, the stratified structure breaks down, allowing sediment to become distributed over the vertical. Hence, sediment export takes place in both the bottom and the surface layers. Instantaneous sediment import through the bottom layer is high in the New Waterway due to flood velocities in the bottom layer being higher than ebb velocities. Next to the asymmetry in tidal currents, however, there exists an asymmetry in tidal duration, with the ebb and LWS phases being considerably longer than the flood and HWS phase (∼8 hours and less than 5 hours respectively). Consequently, the period of seaward transport exceeds the period of landward transport.

3.5 Effect of mixing

Geyer and Ralston (2011) describe how the salinity structure collapses during the ebb phase: supercritical flow at the start of the ebb phase causes shear instabilities, leading to mixing across the pycnocline and initializing the break-down of the salt wedge. As the ebb flow progresses and near-bottom currents increase, turbulence caused by bottom friction overwhelms the internal shear instabilities, causing the collapse of the salinity structure. Also in the New Waterway, diahaline mixing intensifies as ebb progresses, both during neap tide and spring tide. This is visible in the increasing mixing layer thickness (figures 6 and 7 as well as A1 and A2), and in decreasing Richardson gradient-numbers (figure **??**). After the initial shear-induced mixing phase, seaward advection of the salt

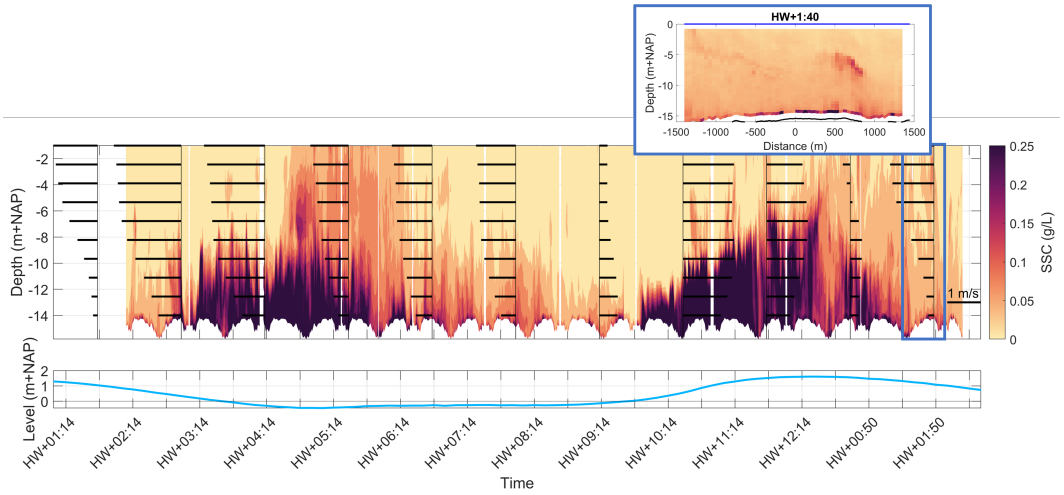

Figure 10. Tidal currents and suspended sediment concentration (top panel) as measured during the neap tidal cycle. Corresponding water levels are provided in the lower panel. Note the different color scale compared to figure 9. An inset shows the elevated SSCs in the upper water layer at the start of the ebb phase.

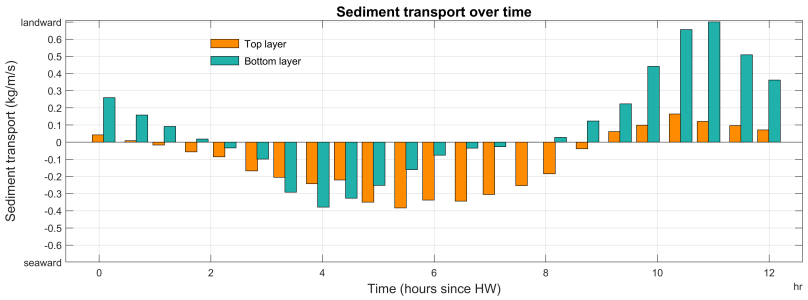

Figure 11. Spatially averaged sediment transport along the longitudinal transect throughout the neap tidal cycle. The top layer and bottom layer are separated by the time-varying interface height z_i.

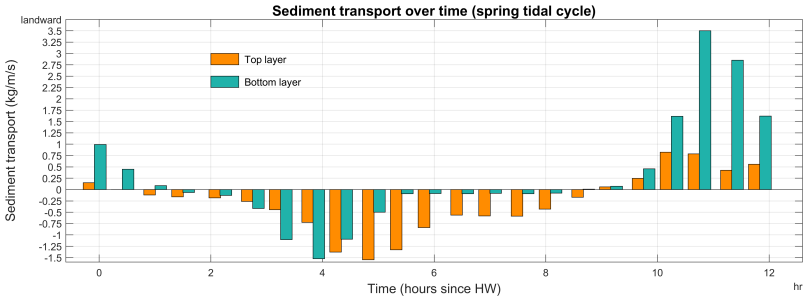

Figure 12. Spatially averaged sediment transport along the longitudinal transect throughout the spring tidal cycle. The top layer and bottom layer are separated by the time-varying interface height z_i. Note the difference in scale with respect to figure 11.

wedge has lowered the pycnocline such that diahaline mixing increases by virtue of bottom-generated shear. Both mixing by interfacial shear instability and by interaction with bottom-generated shear affect the sediment flux in favor of export. Initial shear instability across the density interface is likely to have caused the observed sediment patches in the upper layer (figures 9 and 10). While sediment is still being imported in the bottom layer, shear instability is a likely cause of the diahaline flux of sediment-rich water from the bottom layer into the upper layer, where suspended sediment clouds are then advected seaward. This effect is also visible in figure 11 around t=HW+1:40h, when sediment export by the upper layer exceeds sediment import by the lower layer. Even during spring tide around HW+1:30 (figure 10 or figure 12 around 18:30) sediment transport in the upper layer is relatively high. During the first hours of the ebb period, the observed shear is still very low around the pycnocline in the measuring area. This confirms observations by de Nijs et al. (2011), who reasoned that shear-induced mixing is mostly limited to the head of the salt wedge, which they attributed to the larger baroclinic gradients at the head. This shear-induced mixing thus occurs upstream of our survey area, after which sediment-rich water is advected downstream. In this process, the stratified structure in our measuring area remains largely intact.

As the ebb progresses, the salt wedge retreats and the position of the pycnocline lowers until the region of interfacial shear overlaps with the bottom boundary layer. Diahaline mixing then intensifies by the increasing effect of bottom-generated turbulence. As a result, SSCs are mixed higher into the water column. The effect on suspended sediment transport becomes clear in Figures 11 and 12. During the flood period in the spring and neap tidal cycles, sediment transport in the bottom layer exceeds that in the surface layer by far. In contrast, sediment transport in both layers have the same order of magnitude during the ebb, due to vertical mixing and the high ebb currents in the upper layer. The residual seaward flux of sediment is thus the result of ebb-dominant tidal mixing. This agrees with the findings of Scully and Friedrichs (2003), who found that a residual sediment import in the York River Estuary was partly due to enhanced tidal mixing during the flood period. While the initial shear instabilities and the resulting suspended sediment patches observed in the top layer insignificantly contribute to the residual export, strong mixing during ebb does substantially increase suspended sediment export. Ebb-dominant mixing in combination with a long ebb duration here leads to a dominant ebb flux of sediment.

3.6 Residual transport of suspended sediment

The resulting fluxes along the cross-section are shown in figure 13. The effect of gravitational circulation on sediment transport is significant in both cycles, with net import in the bottom layer and net export in the surface layer. The residual flux is directed seaward in both spring and neap tidal cycles, i.e. there is a net export of suspended sediment. The total export over the spring tidal cycle is $4.3{\cdot}10^6$ kg; the total export over the neap cycle amounts $1.6 \cdot 10^6$ kg.

4 Discussion

4.1 Ebb-mixing and residual sediment transport in estuaries

Festa and Hansen (1978) were among the first to systematically demonstrate that an increasing estuarine circulation increases trapping of marine sediment. Dronkers (1986) further describes the effect of tidal asymmetry on the residual sediment flux which Guo et al. (2014) confirm with a systematic model study: flood dominance increases landward sediment transport, whereas ebb dominance favors seaward residual transport due to the non-linear dependency of sediment transport to velocity. Other systems where a residual landward sediment transport is attributed to (amongst others) flood tidal dominance include the Gironde estuary (Allen et al., 1980), Ems estuary (Chernetsky et al., 2010)

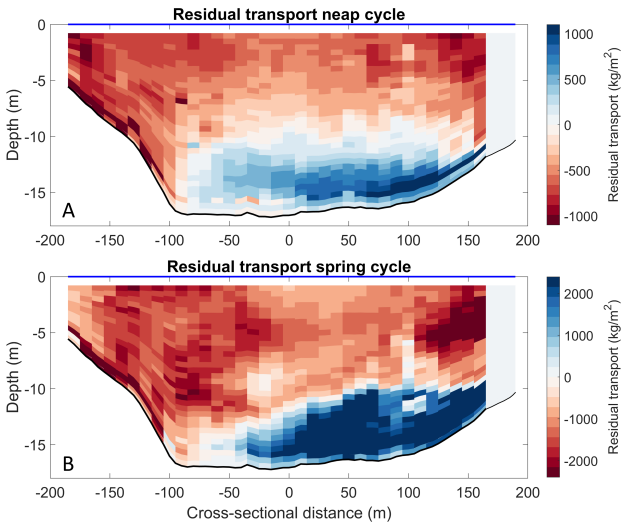

Figure 13. Width- and depth-varying residual sediment transport during neap tide (A) and spring tide (B) at the western transect. Transport at the southern edge (cross-sectional distance between 165 and 190 m) was neglected due to limited data availability. Note that colour scales differ between panel A and panel B.

and parts of the Western Scheldt (Wang et al., 2002). These systems can all be classified as partially mixed or well-mixed in the estuarine classification system proposed by Geyer and MacCready (2014). The York river estuary (Scully & Friedrichs, 2003) can also be classified as partially mixed. Our results from the New Waterway illustrate that in salt-wedge systems, the controls on residual sediment transport are different.

A time-dependent salt wedge estuary is strongly forced by both tides and freshwater flow. As a result, intratidal variations in salinity structure are the result of the large tidal excursion length rather than of tidal mixing during flood. The suppression of tidal mixing leads to high vertical shears in salt-wedge estuaries, especially when tidal currents are strong. Vertical shears during flood can be limited, due to maximum flood velocities being located at mid-depth near the pycnocline. At maximum ebb in the New Waterway, when upper layer velocities are reinforced by the ebb tidal forcing and lower layer velocities are near zero due to the strong baroclinic pressure, vertical shear over the pycnocline reaches its maximum. The same was observed in the Fraser estuary (Geyer & Farmer, 1989), Amazon river mouth (Geyer, 1995) and Merrimack estuary (Geyer et al., 2008), which were all classified as time-dependent salt-wedge systems by Geyer and MacCready (2014). Ralston et al. (2010) emphasizes the additional role of bottom friction as a driver of vertical mixing in the Merrimack estuary as the salt wedge retreats and lowers to interact with the bottom boundary layer during late ebb. Ebb-dominant mixing is thus particularly prominent in salt-wedge and highly stratified estuaries, with both a strong freshwater inflow and strong tidal forcing. While the maximum sediment transport rate in the flood direction exceeds the maximum transport rate in the ebb direction, the long ebb phase of the surface layer in particular results in a tidally averaged seaward transport. The asymmetry in tidal mixing contributes to sediment export by increasing the vertical suspension height of sediment during ebb. We infer that the observed asymmetry in mixing and asymmetry in tidal duration are the main drivers of the seaward residual flux.

One requirement for a time-dependent salt wedge is thus a freshwater inflow which is strong enough to compensate for tidal mixing. The upstream river discharge enter-

ing the Rhine-Meuse Estuary fluctuates within a year, ranging from discharges two times lower to two to three times higher than the average conditions. At the time of our measurements, river discharge was near average. As stated by Guo et al. (2014), a higher river discharge can increase the ebb transport capacity of an estuary. Also, the upstream sediment supply may increase. However, a higher river discharge also impacts the degree of mixing, enhancing vertical stability (Geyer & MacCready, 2014). The net effect of a varying river discharge may be a delicate balance between those factors.

4.2 Residual sediment transport in the New Waterway

Both the neap tidal cycle and the spring tidal cycle show a net export of sediment. This is different from what could be expected from the increasing dredging volumes in the Rhine-Meuse estuary (Cox et al., 2021), and previous sediment budget studies of the area. Both Cox et al. (2021) (based on Becker (2015), Snippen et al. (2005) and van Dreumel (1995)) and Frings et al. (2019) suggest a long-term averaged marine import of both silt ($=< 0.63$ μm) and sand (> 0.64 μm). The derived fluxes from both studies are uncertain as they rely on indirect measurements. The residual flux derived in this study covers only sediment which is transported in suspension, and includes mostly silt and fine sand (< 0.5 mm). Cox et al. (2021) found an annual import of marine silt of 1.83 Mt.

The residual cross-sectional sediment flux found in this study is equivalent to -1.12 Mt per year (neap tide) or -3.03 Mt per year (spring tide). The disparity between these two observed cycles underscores the substantial temporal variability of the residual flux, with a 2.7-fold difference between spring and neap tides, despite consistent river discharge and moderately varying wind conditions during the measuring days. A short period of strong wind occurred 4 days prior to the measured spring cycle with maximum wind speeds of $\approx$19 m/s, resulting in $\approx$ 1 m setup. This may have affected the upstream sediment availability, as the magnitude and direction of the sediment flux is affected by temporally fluctuating flow and weather conditions. Verlaan and Spanhoff (2000) concluded that the import of marine sediment is mostly governed by (storm) events with a frequency of several times per year. Our results also show the impact of geometrical features, as the streamwise spatial variation of the instantaneous sediment flux in the New Waterway is significant. In the longitudinal transects, the effect of narrowing is clearly visible in elevated SSCs during periods of strong flow (figures B1 and B2), which can be attributed to increased resuspension as a result of locally increased flow velocity. Also, the channel bend downstream of our measuring area results in lateral variation of residual sediment transport. A helical flow structure is visible in the residual transport profile along the cross-section (figure 13). This effect is most pronounced in the spring residual profile, due to the higher flow velocities. Since the residual sediment transport is the result of a delicate balance between estuarine circulation, tidal asymmetry and internal asymmetry, and is affected by temporally varying flow and weather conditions, the calculated residual transport values (section 3.6) cannot readily be used to estimate the yearly sediment flux.

4.3 Implications for estuarine development

Mixing asymmetry is thus an important factor determining residual sediment transport in estuaries (Scully & Friedrichs, 2003). Flood-dominant mixing favours sediment import, whereas ebb-dominant mixing favours sediment export. There are two distinct mechanisms which increase vertical mixing during flood (Jay & Musiak, 1996). First, tidal straining intensifies density stratification during ebb. With the velocity maximum located in the upper half of the water column, fresh water is advected over the slower moving saline water near the bottom. During flood, the process is reversed, and the homogeneous vertical density profile is restored (Simpson et al., 1990). Even in the absence of initial vertical mixing, tidal straining increases vertical stability during ebb, and vice versa, during flood. Second, in case of a freshwater outflow, baroclinic and barotropic forces

work in the same direction during ebb, while they act in opposite direction during flood. This results in a layer of increased shear at the pycnocline, favouring mixing during flood. In the New Waterway, the flood velocity vertical maximum coincides with the height of the pycnocline, reducing the shear and local turbulence production at the pycnocline. During the long ebb period, the pycnocline lowers, allowing bottom-generated turbulence to break up the vertical density structure.

Similar cases of ebb-dominant mixing were found for the Merrimack River (Ralston et al., 2010) and the Fraser River Estuary (Geyer & Farmer, 1989). In both cases, the increased mixing during ebb was attributed to a decreasing pycnocline height, leading to interaction with the turbulent bottom boundary layer. The current trend of fairway deepening in deltas worldwide may result in more stratified systems, as the relative strength of tidal mixing decreases (Geyer & MacCready, 2014). Additionally, in systems with a strong tidal forcing, gravitational circulation may strengthen as a result of deepening, leading to more import of marine sediment.

4.4 Implications for modelling of estuarine sediment transport

Our study highlights the impact of vertical mixing on residual sediment transport. While the role of vertical mixing is small compared to the classical mechanisms explaining sediment import (gravitational circulation and flood dominance (Burchard et al., 2018)) and sediment export (river discharge and ebb dominance (Guo et al., 2014)), we show here that asymmetric mixing can significantly contribute to a residual sediment flux that is opposite to what may be expected based on the main indicators. This implies that depth-averaged estuarine models such as deployed by Guo et al. (2014) are of limited applicability for time-dependent salt wedge systems.

5 Conclusions

Based on field data, we investigated the main drivers of residual sediment transport in a channelized time-dependent salt wedge estuary. We found that the residual flux is directed landward, despite a strong near-bed flood-dominance. We find that the long ebb period which is associated with flood dominance results in a seaward residual sediment flux. Two mixing mechanisms explain this: 1) Initial entrainment of sediment-rich marine water into the seaward flowing fresh water layer likely due to shear instabilities over the pycnocline and 2) a larger resuspension height during the ebb phase, associated with a higher degree of mixing. The first mechanism only has a minor impact on the total residual flux. The latter mechanism (ebb-dominant mixing), is characteristic for time-dependent salt wedge estuaries around the world, and favours a seaward residual sediment flux. We thus conclude that, while the residual sediment flux is traditionally assumed to be governed by gravitational circulation and barotropic asymmetry, internal asymmetry has an additional impact on the residual sediment flux that cannot be neglected in time-dependent salt wedges.

Data availability statement

All field data will be made available in the 4TU-repository once the article is accepted (data.4tu.nl; link will be made available upon publication). We processed the data using matlab. All scripts to process the field data and create the figures will be uploaded into the repository. For processing the raw ADCP-data, the "adcptools"-toolbox was used, which is publicly available at Github (github.com/bartverm/adcptools). All meteorological and water level data used in this study were publicly available from Rijkswaterstaat (www.waterinfo.nl) and the Royal Netherlands Meteorological Institute (www.knmi.nl/nederland-nu/klimatologie/uurgegevens).

Acknowledgments

This study is part of the research program Rivers2Morrow, which is funded by the Dutch Ministry of Infrastructure and Water Management and its executive organization Rijkswaterstaat. We thank the Port of Rotterdam for their in-kind contribution and support with the field measurements. We greatly thank Henk Jongbloed for his help with the processing of our data. Additionally, we thank Judith Zomer and David Boelee for their help in organizing and carrying out the measurements.

Appendix A Results of the salinity profile fit

Appendix B Longitudinal transects

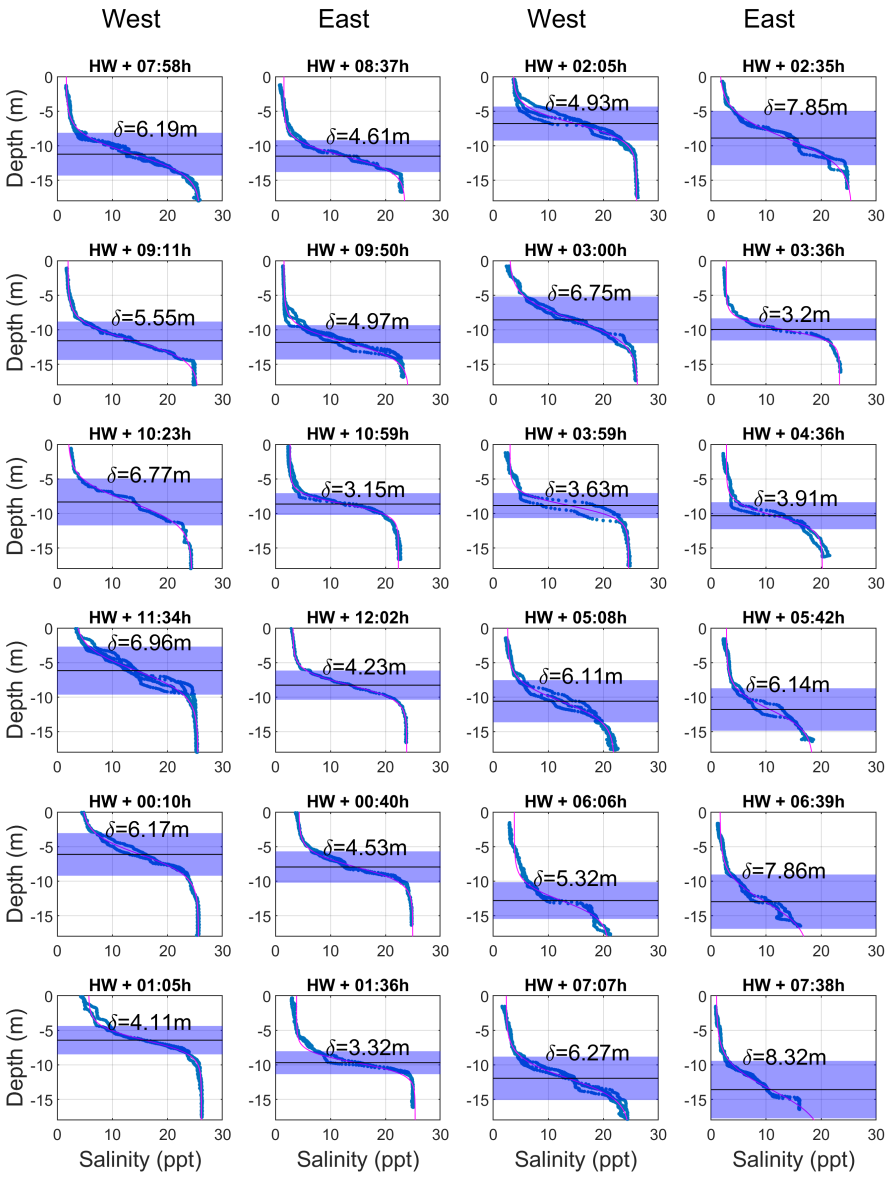

Figure A1. Vertical salinity profiles resulting from the CTD-casts (blue points) and the fitted sigmoid-profile (black line) during the neap tidal cycle. The shaded area indicated the location and thickness of the mixing layer. Title indicates the time in hours relative to HWS.

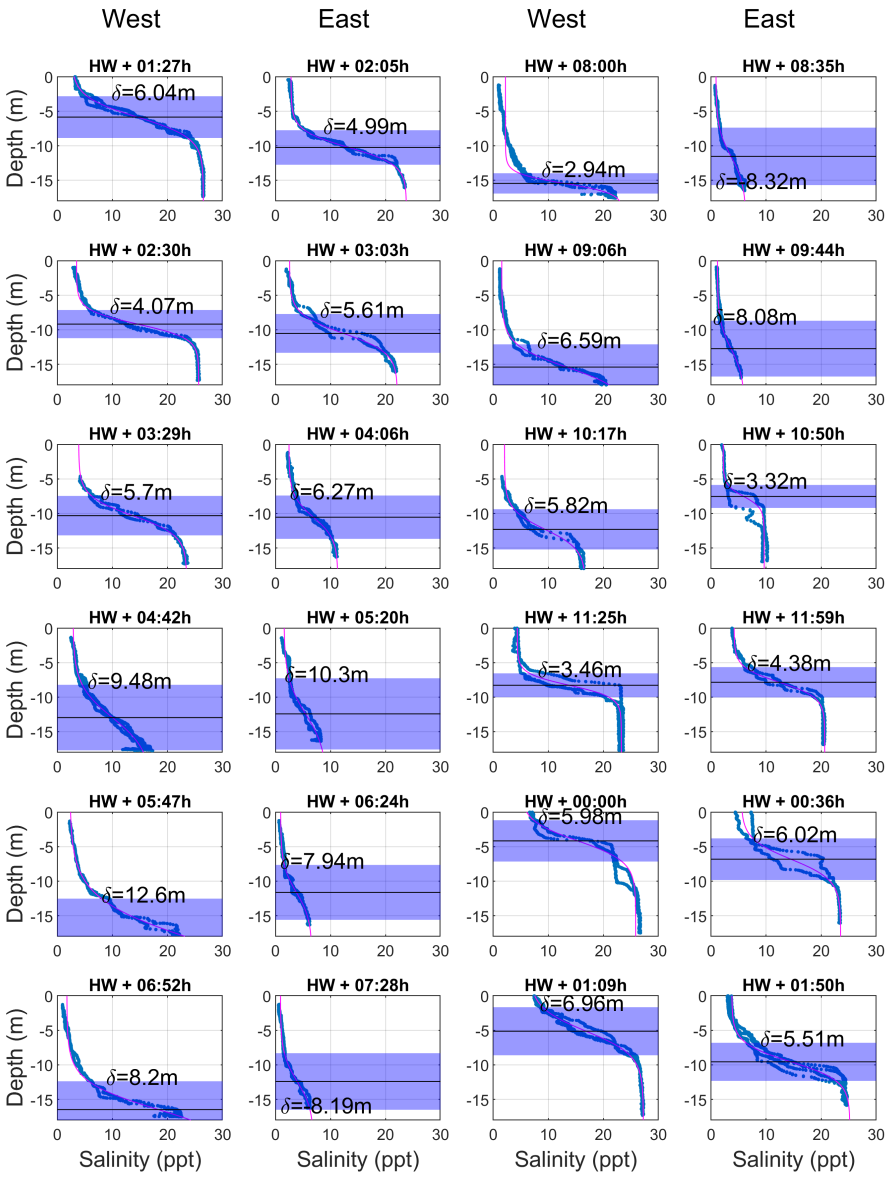

Figure A2. Vertical salinity profiles resulting from the CTD-casts (blue points) and the fitted sigmoid-profile (black line) during the spring tidal cycle. The shaded area indicated the location and thickness of the mixing layer. Title indicates the time in hours relative to HWS.

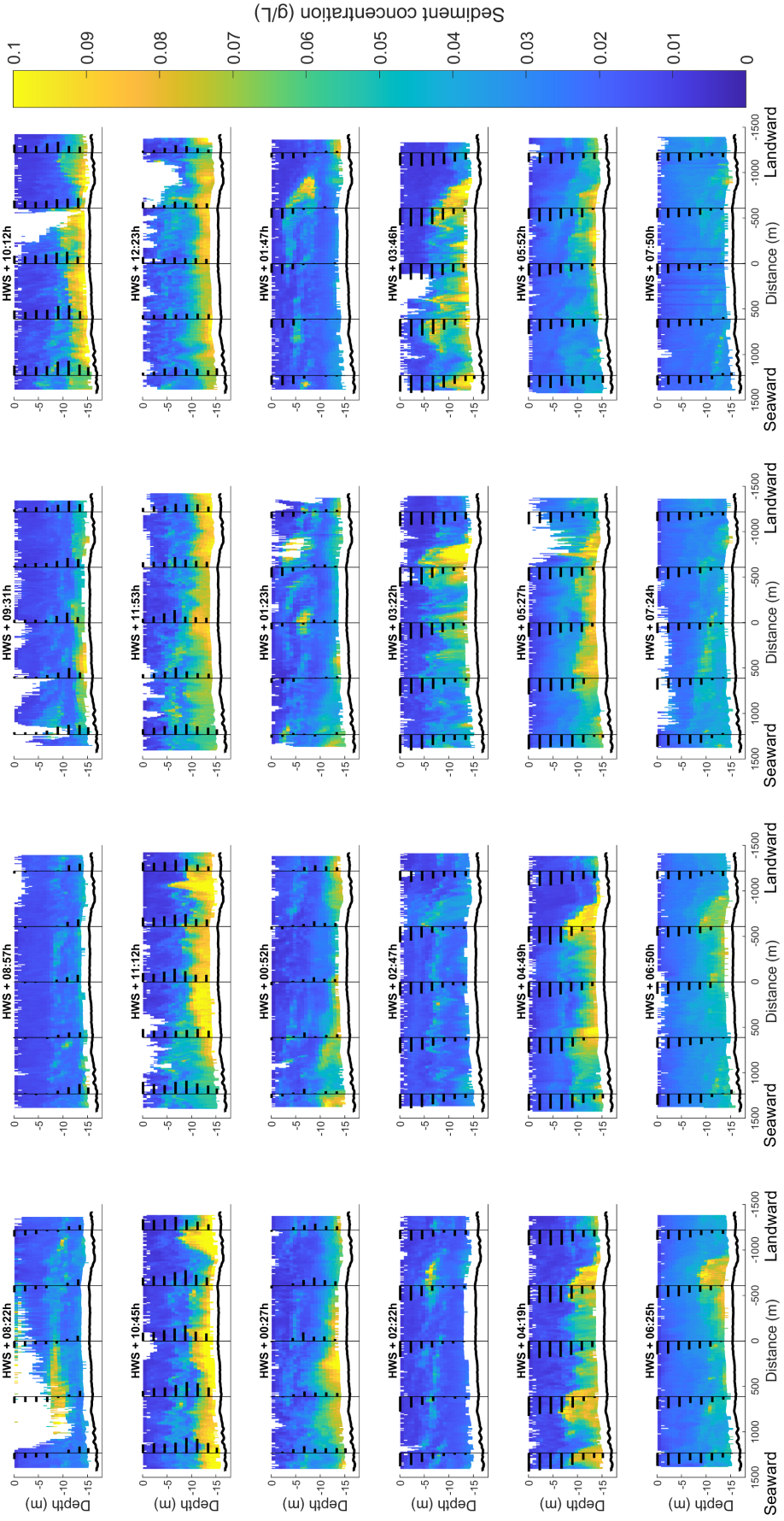
Sediment concentration (g/L)
0.1
0.09
0.08
0.07
0.06
0.05
0.04
0.03
0.02
0.01
0
HWS + 08:22h
HWS + 08:57h
HWS + 09:31h
HWS + 10:12h
HWS + 10:45h
HWS + 11:12h
HWS + 11:53h
HWS + 12:23h
HWS + 00:27h
HWS + 00:52h
HWS + 01:23h
HWS + 01:47h
HWS + 02:22h
HWS + 02:47h
HWS + 03:22h
HWS + 03:46h
HWS + 04:19h
HWS + 04:49h
HWS + 05:27h
HWS + 05:52h
HWS + 06:25h
HWS + 06:50h
HWS + 07:24h
HWS + 07:50h
Depth (m)
Distance (m)
Seaward
Landward

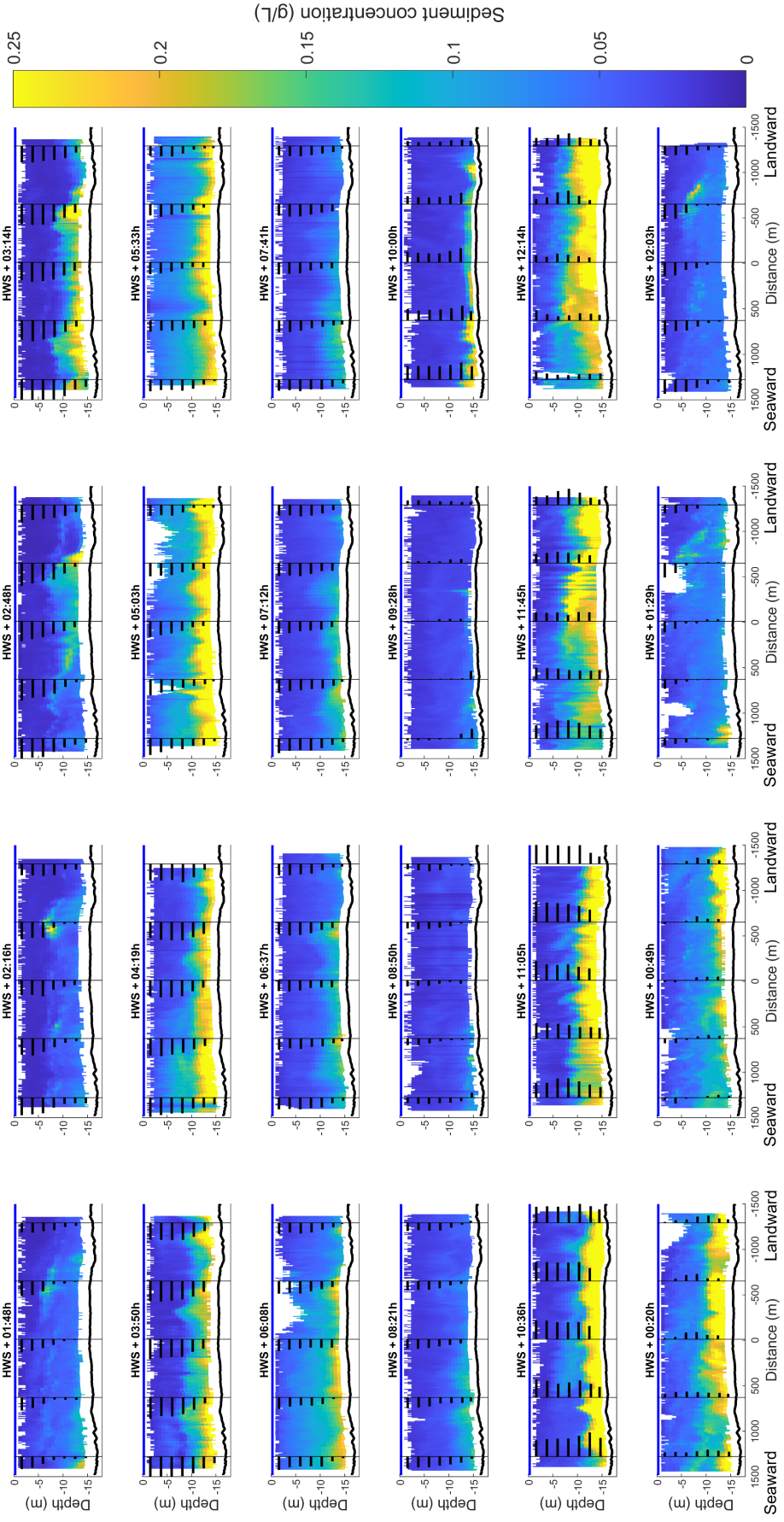
Sediment concentration (g/L)
0.25
0.2
0.15
0.1
0.05
0
HWS + 01:48h
HWS + 02:16h
HWS + 02:48h
HWS + 03:14h
HWS + 03:50h
HWS + 04:19h
HWS + 05:03h
HWS + 05:33h
HWS + 06:08h
HWS + 06:37h
HWS + 07:12h
HWS + 07:41h
HWS + 08:21h
HWS + 08:50h
HWS + 09:28h
HWS + 10:00h
HWS + 10:36h
HWS + 11:05h
HWS + 11:45h
HWS + 12:14h
HWS + 00:20h
HWS + 00:49h
HWS + 01:29h
HWS + 02:03h
Depth (m)
Seaward
Distance (m)
Landward

References

Allen, G. P., Salomon, J. C., Bassoullet, P., Du Penhoat, Y., & de Grandpré, C. (1980, April). Effects of tides on mixing and suspended sediment transport in macrotidal estuaries. *Sedimentary Geology*, *26*(1), 69–90. doi: 10.1016/0037-0738(80)90006-8

Becker, A. (2015, September). *Sediment in (be)weging* (Tech. Rep. No. 1208925-000-ZWS-0023). Delft: Deltares.

Burchard, H., Schuttelaars, H. M., & Ralston, D. K. (2018, January). Sediment Trapping in Estuaries. *Annual Review of Marine Science*, *10*(1), 371–395. doi: 10.1146/annurev-marine-010816-060535

Canestrelli, A., Lanzoni, S., & Fagherazzi, S. (2014, March). One-dimensional numerical modeling of the long-term morphodynamic evolution of a tidally-dominated estuary: The Lower Fly River (Papua New Guinea). *Sedimentary Geology*, *301*, 107–119. doi: 10.1016/j.sedgeo.2013.06.009

Chant, R. J., & Stoner, A. W. (2001). Particle trapping in a stratified flood-dominated estuary. *Journal of Marine Research*.

Chernetsky, A. S., Schuttelaars, H. M., & Talke, S. A. (2010, October). The effect of tidal asymmetry and temporal settling lag on sediment trapping in tidal estuaries. *Ocean Dynamics*, *60*(5), 1219–1241. doi: 10.1007/s10236-010-0329-8

Cox, J. R., Huismans, Y., Knaake, S. M., Leuven, J. R. F. W., Vellinga, N. E., Vegt, M., ... Kleinhans, M. G. (2021, July). Anthropogenic Effects on the Contemporary Sediment Budget of the Lower Rhine-Meuse Delta Channel Network. *Earth's Future*, *9*(7). doi: 10.1029/2020EF001869

de Nijs, M. A. J., & Pietrzak, J. D. (2012, June). Saltwater intrusion and ETM dynamics in a tidally-energetic stratified estuary. *Ocean Modelling*, *49–50*, 60–85. doi: 10.1016/j.ocemod.2012.03.004

de Nijs, M. A. J., Pietrzak, J. D., & Winterwerp, J. C. (2011, January). Advection of the Salt Wedge and Evolution of the Internal Flow Structure in the Rotterdam Waterway. *Journal of Physical Oceanography*, *41*(1), 3–27. doi: 10.1175/2010JPO4228.1

De Nijs, M. a. J. (2012). *On sedimentation processes in a stratified estuarine system* (doctoral thesis, TU Delft, Delft). doi: 10.4233/uuid:fb0ec18d-dcfd-468d-af4a-45bfb02cac1c

Dronkers, J. (1986, August). Tidal asymmetry and estuarine morphology. *Netherlands Journal of Sea Research*, *20*(2), 117–131. doi: 10.1016/0077-7579(86)90036-0

Dronkers, J. (2005). *Dynamics Of Coastal Systems*. Singapore: World Scientific.

Dyer, K. R. (1991, March). Circulation and mixing in stratified estuaries. *Marine Chemistry*, *32*(2), 111–120. doi: 10.1016/0304-4203(91)90031-Q

Dyer, K. R. (1995). Chapter 14 Sediment Transport Processes in Estuaries. In *Developments in Sedimentology* (Vol. 53, pp. 423–449). Elsevier. doi: 10.1016/S0070-4571(05)80034-2

Festa, J. F., & Hansen, D. V. (1978, October). Turbidity maxima in partially mixed estuaries: A two-dimensional numerical model. *Estuarine and Coastal Marine Science*, *7*(4), 347–359. doi: 10.1016/0302-3524(78)90087-7

Frings, R. M., Hillebrand, G., Gehres, N., Banhold, K., Schriever, S., & Hoffmann, T. (2019, September). From source to mouth: Basin-scale morphodynamics of the Rhine River. *Earth-Science Reviews*, *196*, 102830. doi: 10.1016/j.earscirev.2019.04.002

Geyer, W. (1995, February). Tide-induced mixing in the Amazon Frontal Zone. *Journal of Geophysical Research: Oceans*, *100*(C2), 2341–2353. doi: 10.1029/94JC02543

Geyer, W., & Farmer. (1989, August). Tide-Induced Variation of the Dynamics of a Salt Wedge Estuary. *Journal of Physical Oceanography*, *19*(8), 1060–1072. doi: 10.1175/1520-0485(1989)019⟨1060:TIVOTD⟩2.0.CO;2

Geyer, W., & MacCready, P. (2014). The Estuarine Circulation. *Annual Review of Fluid Mechanics*, *46*(1), 175–197. doi: 10.1146/annurev-fluid-010313-141302

Geyer, W., & Ralston, D. (2011). The Dynamics of Strongly Stratified Estuaries. In *Treatise on Estuarine and Coastal Science* (pp. 37–51). Elsevier. doi: 10.1016/B978-0-12-374711-2.00206-0

Geyer, W., Scully, M., & Ralston, D. (2008, December). Quantifying vertical mixing in estuaries. *Environmental Fluid Mechanics*, *8*(5-6), 495–509. doi: 10.1007/s10652-008-9107-2

Gostiaux, L., & van Haren, H. (2010, May). Extracting Meaningful Information from Uncalibrated Backscattered Echo Intensity Data. *Journal of Atmospheric and Oceanic Technology*, *27*(5), 943–949. doi: 10.1175/2009JTECHO704.1

Guo, L., Brand, M., Sanders, B. F., Foufoula-Georgiou, E., & Stein, E. D. (2018, November). Tidal asymmetry and residual sediment transport in a short tidal basin under sea level rise. *Advances in Water Resources*, *121*, 1–8. doi: 10.1016/j.advwatres.2018.07.012

Guo, L., van der Wegen, M., Roelvink, J. A., & He, Q. (2014). The role of river flow and tidal asymmetry on 1-D estuarine morphodynamics. *Journal of Geophysical Research: Earth Surface*, *119*(11), 2315–2334. doi: 10.1002/2014JF003110

Huismans, Y., Koopmans, H., Wiersma, A., de Haas, T., Berends, K., Sloff, K., & Stouthamer, E. (2021, July). Lithological control on scour hole formation in the Rhine-Meuse Estuary. *Geomorphology*, *385*, 107720. doi: 10.1016/j.geomorph.2021.107720

Jay, D. A., & Musiak, J. D. (1996). Internal Tidal Asymmetry in Channel Flows: Origins and Consequences. In *Mixing in Estuaries and Coastal Seas* (pp. 211–249). American Geophysical Union (AGU). doi: 10.1029/CE050p0211

Jongbloed, H., Vermeulen, B., & Hoitink, A. (2023). *Physics-informed estimation of open channel flow fields from acoustic Doppler current profiler transect data.* Submitted to Water Resources Research.

Leuven, J. R. F. W., Niesten, I., Huismans, Y., Cox, J. R., Hulsen, L., van der Kaaij, T., & Hoitink, A. J. F. T. (2023). Peak Water Levels Rise Less Than Mean Sea Level in Tidal Channels Subject to Depth Convergence by Deepening. *Journal of Geophysical Research: Oceans*, *128*(4), e2022JC019578. doi: 10.1029/2022JC019578

Miles, J. W. (1961, June). On the stability of heterogeneous shear flows. *Journal of Fluid Mechanics*, *10*(04), 496. doi: 10.1017/S0022112061000305

Pugh, D., & Woodworth, P. (2014). *Sea-level science: Understanding tides, surges, tsunamis and mean sea-level changes* (2nd ed ed.). Cambridge: Cambridge university press.

Ralston, D. K., Geyer, W. R., Lerczak, J. A., & Scully, M. (2010, December). Turbulent mixing in a strongly forced salt wedge estuary. *Journal of Geophysical Research*, *115*(C12), C12024. doi: 10.1029/2009JC006061

Richardson, L. F., & Shaw, W. N. (1920, July). The supply of energy from and to atmospheric eddies. *Proceedings of the Royal Society of London. Series A, Containing Papers of a Mathematical and Physical Character*, *97*(686), 354–373. doi: 10.1098/rspa.1920.0039

Sassi, M. G., Hoitink, A. J. F., & Vermeulen, B. (2012). Impact of sound attenuation by suspended sediment on ADCP backscatter calibrations. *Water Resources Research*, *48*(9). doi: 10.1029/2012WR012008

Schijf, J. B., & Schönfeld, J. C. (1953). Theoretical considerations on the motion of salt and fresh water. *Proceedings Minnesota International Hydraulic Convention*.

Scully, M. E., & Friedrichs, C. T. (2003, September). The influence of asymmetries in overlying stratification on near-bed turbulence and sediment suspension in a partially mixed estuary. *Ocean Dynamics*, *53*(3), 208–219. doi: 10.1007/s10236-003-0034-y

Scully, M. E., & Friedrichs, C. T. (2007). Sediment pumping by tidal asymmetry in a partially mixed estuary. *Journal of Geophysical Research: Oceans*, *112*(C7). doi: 10.1029/2006JC003784

Simpson, J. H., Brown, J., Matthews, J., & Allen, G. (1990). Tidal Straining, Density Currents, and Stirring in the Control of Estuarine Stratification. *Estuaries*, *13*(2), 125–132. doi: 10.2307/1351581

Snippen, E., Fioole, A., Geelen, H., Kamsteeg, A., Van Spijk, A., & Visser, T. (2005, May). *Sediment in (be)weging. Sedimentbalans Rijn-Maasmonding periode 1990-2000.* (Technical Report). Rijkswaterstaat-RIZA.

Stacey, M. T., Monismith, S. G., & Burau, J. R. (1999, August). Observations of Turbulence in a Partially Stratified Estuary. *Journal of Physical Oceanography*, *29*(8), 1950–1970. doi: 10.1175/1520-0485(1999)029⟨1950:OOTIAP⟩2.0.CO;2

Trowbridge, J. H. (1992). A simple description of the deepening and structure of a stably stratified flow driven by a surface stress. *Journal of Geophysical Research: Oceans*, *97*(C10), 15529–15543. doi: 10.1029/92JC01512

UNESCO/IOC. (2010). *The international thermodynamic equation of seawater – 2010: Calculation and use of thermodynamic properties* (Intergovernmental Oceanographic Commission, Manuals and Guides No. 56).

van Dreumel, P. (1995, December). *Slib- en zandbeweging in het noordelijk Deltabekken in de periode 1982-1992.* (Tech. Rep.). Rotterdam: D.G. Rijkswaterstaat: Afdeling Watersysteemkennis.

Vellinga, N. E., Hoitink, A. J. F., van der Vegt, M., Zhang, W., & Hoekstra, P. (2014, August). Human impacts on tides overwhelm the effect of sea level rise on extreme water levels in the Rhine–Meuse delta. *Coastal Engineering*, *90*, 40–50. doi: 10.1016/j.coastaleng.2014.04.005

Verlaan, P. A. J., & Spanhoff, R. (2000). Massive Sedimentation Events at the Mouth of the Rotterdam Waterway. *Journal of Coastal Research*, *16*(2), 458–469.

Vermeulen, B., & Jongbloed, H. (2023). *adcptools* [software]. GitHub. Retrieved from `https://github.com/bartverm/adcptools` (v1.0, accessed September 14th, 2023)

Vermeulen, B., Sassi, M. G., & Hoitink, A. J. F. (2014, May). Improved flow velocity estimates from moving-boat ADCP measurements. *Water Resources Research*, *50*(5), 4186–4196. doi: 10.1002/2013WR015152

Wang, Z. B., Jeuken, M. C. J. L., Gerritsen, H., de Vriend, H. J., & Kornman, B. A. (2002, November). Morphology and asymmetry of the vertical tide in the Westerschelde estuary. *Continental Shelf Research*, *22*(17), 2599–2609. doi: 10.1016/S0278-4343(02)00134-6